

---

# Detailed modeling of dust distribution in the disk of HD 142527

Kang-Lou SOON<sup>1,\*</sup>, Tomoyuki HANAWA<sup>2</sup>, Takayuki MUTO<sup>3</sup>,

Takashi TSUKAGOSHI<sup>1</sup>, and Munetake MOMOSE<sup>1,4</sup>

<sup>1</sup>College of Science, Ibaraki University, 2-1-1 Bunkyo, Mito 310-8512, Japan

<sup>2</sup>Center for Frontier Science, Chiba University, 1-33 Yayoi-cho, Inage-ku, Chiba 263-8522, Japan

<sup>3</sup>Division of Liberal Arts, Kogakuin University, 1-24-2 Nishi-Shinjuku, Shinjuku-ku, Tokyo 163-8677, Japan

<sup>4</sup>Visiting Professor, National Astronomical Observatory of Japan, 2-21-1 Osawa, Mitaka, Tokyo, 181-8588, Japan

\*E-mail: 14nd402n@vc.ibaraki.ac.jp

Received (reception date); Accepted (acceptation date)

## Abstract

We investigate the dust distribution in the crescent disk around HD 142527 based on the continuum emission at  $890 \mu\text{m}$  obtained by ALMA Cycle 0. The map is divided into 18 azimuthal sectors, and the radial intensity profile in each sector is reproduced with a 2D disk model. Our model takes account of scattering and inclination of the disk as well as the azimuthal dependence in intensity. When the dust is assumed to have the conventional composition and maximum size of 1 mm, the northwestern region ( $PA = 291^\circ - 351^\circ$ ) cannot be reproduced. This is because the model intensity gets insensitive to the increase in surface density due to heavy self-scattering, reaching its ceiling much lower than the observed intensity. The ceiling depends on the position angle. When the scattering opacity is reduced by a factor of 10, the intensity distribution is reproduced successfully in all the sectors including those in the northwestern region. The best fit model parameters depend little on the scattering opacity in the southern region where the disk is optically thin. The contrast of dust surface density along  $PA$  is derived to be about 40, much smaller than the value for the cases of conventional opacities

(70 – 130). These results strongly suggest that the albedo is lower than considered by some reasons at least in the northwestern region.

**Key words:** radiative transfer — stars: individual (HD 142527) — star: pre-main sequence — protoplanetary disks — submillimeter: planetary systems

---

## 1 Introduction

Transitional disks are believed to be in an evolutionary stage from a gas-rich, primordial phase to a gas-poor, debris phase. Unlike the primordial disks with large emission excess between  $2\ \mu\text{m}$  and  $25\ \mu\text{m}$ , their spectral energy distributions show a dip at around  $5\ \mu\text{m}$ , signifying little or no emission excess in this near-infrared regime (Strom et al. 1989; Skrutskie et al. 1990; Muzerolle et al. 2010; Andrews et al. 2011; Williams & Cieza 2011; Espaillat et al. 2014). From the early modeling (Calvet et al. 2002; Calvet et al. 2005) and the recent high-angular resolution imaging at infrared and (sub-)millimeter wavelengths, the dip is indicative of a dust cavity in the disk’s inner region (Brown et al. 2009; Grady et al. 2015).

The continuum emission at millimeter and sub-millimeter wavelengths from the transitional disks is often observed to be azimuthally asymmetric (Isella et al. 2013; van der Marel et al. 2013; Pérez et al. 2014). The asymmetry is considered to be the consequence of dust accumulation in regions of higher gas pressure. The formation mechanism of such a pressure maximum is still under debate, but it includes a large-scale vortex (Lyra & Lin 2013; Zhu & Stone 2014), the perturbation by an unseen planet in the inner hole (Birnstiel et al. 2013), and a fast gravitational global ( $m = 1$ ) mode in the gas disk (Mittal & Chiang 2015; Baruteau & Zhu 2016). In order to examine the validity of these proposed mechanisms, further information about the disk structure should be provided based on observational results.

HD 142527 is a young Herbig star of spectral type F7III (van den Ancker et al. 1998), surrounded by a transitional disk. Considering its association with Sco OB2, the distance to the star is assumed to be 140 pc. The mass, radius, and the effective temperature of the star are  $2.2 M_{\odot}$ ,  $3.8 R_{\odot}$ , and 6250 K (Fukagawa et al. 2006; Verhoeff et al. 2011; Mendigutía et al. 2014). A companion of  $0.1 M_{\odot} - 0.4 M_{\odot}$  is found at about 13 au from the central star (Biller et al. 2012; Close et al. 2014; Rodigas et al. 2014). The disk structure of HD 142527 has been studied at various wavelengths (Fukagawa et al. 2006; Fujiwara et al. 2006). Sub-millimeter observations yielded the outer disk as a crescent structure with a cavity of the size of approximately 150 au in radius. The continuum emission

in the northern region of the outer disk is brighter, thus more dust-concentrated, than in the southern region (Casassus et al. 2013). On the other hand, the gas distributions revealed by the CO rotational lines are moderately symmetric with respect to the disk rotation axis. From the gas kinematics traced by  $^{13}\text{CO}$  ( $J = 3 - 2$ ), the inclination of the disk axis to the line of sight is derived to be  $27^\circ$  (Fukagawa et al. 2013). A 34 GHz dust clump is seen in the northern region of the disk, strongly suggesting the presence of centimeter-size dust grains (Casassus et al. 2015).

Muto et al. (2015) carried out detailed modeling of dust and gas radial distribution in  $PA = 11^\circ - 31^\circ$  and  $PA = 211^\circ - 231^\circ$ , the brightest and the faintest position angle ( $PA$ ) sectors in the continuum emission. They try to reproduce the radial profiles of the dust continuum emission at  $\lambda = 890 \mu\text{m}$  and line emissions of  $^{13}\text{CO}$  ( $J = 3 - 2$ ) and  $\text{C}^{18}\text{O}$  ( $J = 3 - 2$ ) in the two sectors. Their results are consistent with dust accumulation in pressure maxima; while the contrast of dust surface density along  $PA$  is  $\sim 70$ , that in gas surface density is only  $\sim 4$ . In order to reveal the whole dust distribution that may be the key to understanding the formation mechanism of the crescent structure, we extend the modeling of dust continuum emission in all the  $PA$  directions. We use the same modeling method adopted by Muto et al. (2015).

This paper is organized as follows. In Section 2 we summarize the observational data used in this study. We introduce our modeling procedure in Section 3, and present the results in Section 4. Section 5 is reserved for discussions.

## 2 Observational data

We use the continuum data of HD 142527 taken by ALMA over the period from 2012 June to August (ADS/JAO.ALMA#2011.0.00318.S). Six scheduling blocks were carried out by using the Extended Array Configuration in Cycle 0 consisting of 20 to 26 12-meter antennas, forming a maximum baseline of about 480 m. The correlator was configured to store dual polarizations in four separate spectral windows. The central frequencies for the windows are 330.588, 329.331, 342.883, and 342.400 GHz; each window has a 469 MHz bandwidth over 3840 channels. Aggregating all the line-free channels in the spectral windows, we obtain a 1.8 GHz bandwidth for the continuum data at 336 GHz, or  $\lambda_{\text{obs}} = 890 \mu\text{m}$ . The on-source integration time is three hours after flagging aberrant data.

Calibration and data reduction are made with the Common Astronomy Software Applications package version 3.4. We use Briggs weighting with a robust parameter of 0.5 during the self-calibration, in order to recover the weak and extended components of the dust emission (Muto et al. 2015). The synthesized beam (FWHM) is  $0''.40 \times 0''.47$  ( $PA = 59^\circ.9$ ), or  $56 \text{ au} \times 66 \text{ au}$  at the distance of HD 142527. The RMS noise level is  $0.61 \text{ mJy asec}^{-2}$ . Figure 1 shows the self-calibrated

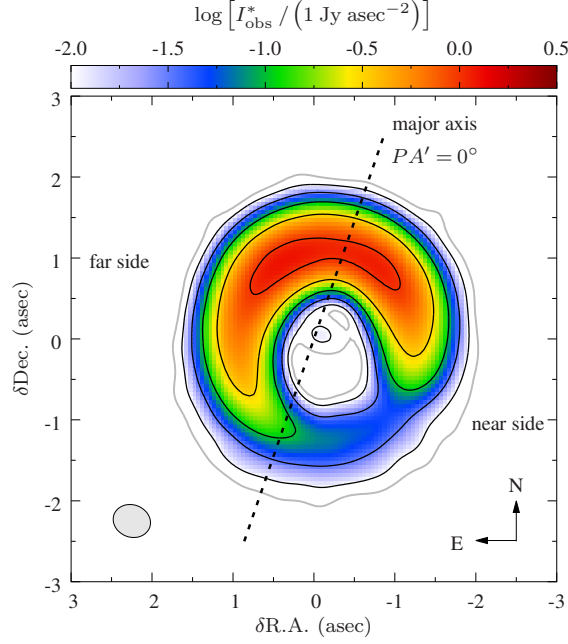


**Fig. 1:** Image of the continuum emission at  $\lambda_{\text{obs}} = 890 \mu\text{m}$  taken with ALMA. Black contours denote the intensity  $I_{\text{obs}}^*$  ( $\text{Jy asec}^{-2}$ ) at  $\log [I_{\text{obs}}^*] = -2.0, -1.5, -1.0, -0.5, 0.0$ . The gray contours denote the intensity at  $5 \sigma$  level ( $1 \sigma = 0.61 \text{ mJy asec}^{-2}$ ). The synthesized beam is shown in the bottom left corner. The far side is in the northeast while the near side is in the southwest.

image of the disk surrounding HD 142527.

As the groundwork in our modeling, we create radial intensity profiles of the continuum emission for 18 azimuthal sectors with a radial bin width of 14 au. We fit these discrete averaged intensities in every sector by using a Gaussian function,

$$I_{\text{obs}}^*(r_{\text{obs}}^*) = I_{0,\text{obs}}^* \exp \left[ - \left( \frac{r_{\text{obs}}^* - r_{0,\text{obs}}^*}{w_{0,\text{obs}}^*} \right)^2 \right], \quad (1)$$

where  $r_{\text{obs}}^*$  denotes the projected radius from the star,  $I_{0,\text{obs}}^*$  the peak intensity at  $r_{0,\text{obs}}^*$ , and  $w_{0,\text{obs}}^*$  the projected width of the radial profile. The results of Gaussian-fitting are listed in table 1. In this paper, we use  $PA'$ , the angle measured from the disk major axis, to denote the azimuthal position of the disk instead of  $PA$ , i.e.,  $PA' = PA + 19^\circ$ . Equation (1) is a function of  $PA'$ , but we have omitted it for convenience.

### 3 Modeling procedure

Our goal is to derive the dust surface density distribution for the disk that reproduces  $I_{0,\text{obs}}^*$ ,  $w_{0,\text{obs}}^*$ , and  $r_{0,\text{obs}}^*$  in each  $PA'$  sector. Since the observed intensity of the disk around HD 142527 varies smoothly in the azimuthal direction, we employ a 2D axisymmetric model as a fiducial model to reproduce the intensity in each sector individually (Muto et al. 2015). The scattered light of the observed crescent

**Table 1:** Gaussian-fitted results for the observed radial intensity profiles.

$PA'$	$I_{0,\text{obs}}^*$ (Jy asec $^{-2}$ )	$w_{0,\text{obs}}^*$ (au)	$r_{0,\text{obs}}^*$ (au)
10° – 30°	1.16	50.9	158.4
30° – 50°	1.25	51.0	152.3
50° – 70°	1.19	50.2	148.6
70° – 90°	0.94	49.0	143.1
90° – 110°	0.72	47.0	142.6
110° – 130°	0.55	45.9	145.2
130° – 150°	0.39	45.5	150.6
150° – 170°	0.22	45.6	159.7
170° – 190°	0.11	46.5	169.5
190° – 210°	0.07	47.8	179.2
210° – 230°	0.06	50.5	178.3
230° – 250°	0.05	51.6	174.1
250° – 270°	0.13	47.9	161.5
270° – 290°	0.34	48.7	158.9
290° – 310°	0.62	48.2	157.9
310° – 330°	0.96	48.5	158.6
330° – 350°	1.16	48.3	160.4
350° – 10°	1.13	49.3	159.9

disk, however, may be different from that of the axisymmetric model when scattering is dominant; the validity of this approach is discussed in Section 5.2.

The dust surface density distribution in the radial ( $r$ ) direction is assumed to be

$$\Sigma(r) = \Sigma_0 \exp \left\{ -\min \left[ \left( \frac{r - r_0}{w_0} \right)^2, 20 \right] \right\}, \quad (2)$$

where  $\Sigma_0$ ,  $w_0$ , and  $r_0$  denote the peak surface density, the radial width of the distribution, and the peak radius, respectively. Note that the floor  $\exp(-20)$  is set for computational convenience. We determine  $(\Sigma_0, w_0, r_0)$  by the following procedure:

1. Compute the surface density distribution,  $\Sigma(r)$ , for given sets of  $(\Sigma_0, w_0, r_0)$ . The model parameters are varied in the range of  $-2.1 \leq \log \Sigma_0$  (g cm $^{-2}$ )  $\leq 0.1$  with the interval  $\Delta \log \Sigma_0 = 0.1$ , in  $21 \text{ au} \leq w_0 \leq 31 \text{ au}$  with  $\Delta w_0 = 2 \text{ au}$ , and in  $159 \text{ au} \leq r_0 \leq 199 \text{ au}$  with  $\Delta r_0 = 8 \text{ au}$ . They are

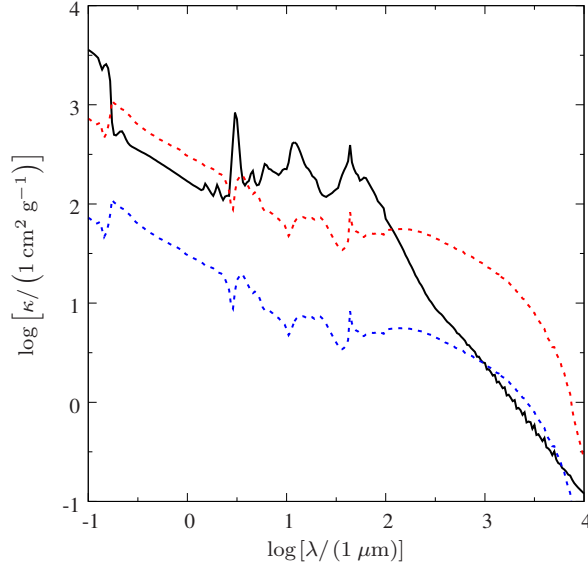


**Fig. 2:** Conventional values of the absorption opacity (black solid line) and the scattering opacity (red dashed line) per unit dust mass, for compact dust grains following distribution  $a^{-3.5}$ , with  $a_{\max} = 1$  mm. The blue dashed line indicates the scattering opacity reduced to 10% from their conventional values.

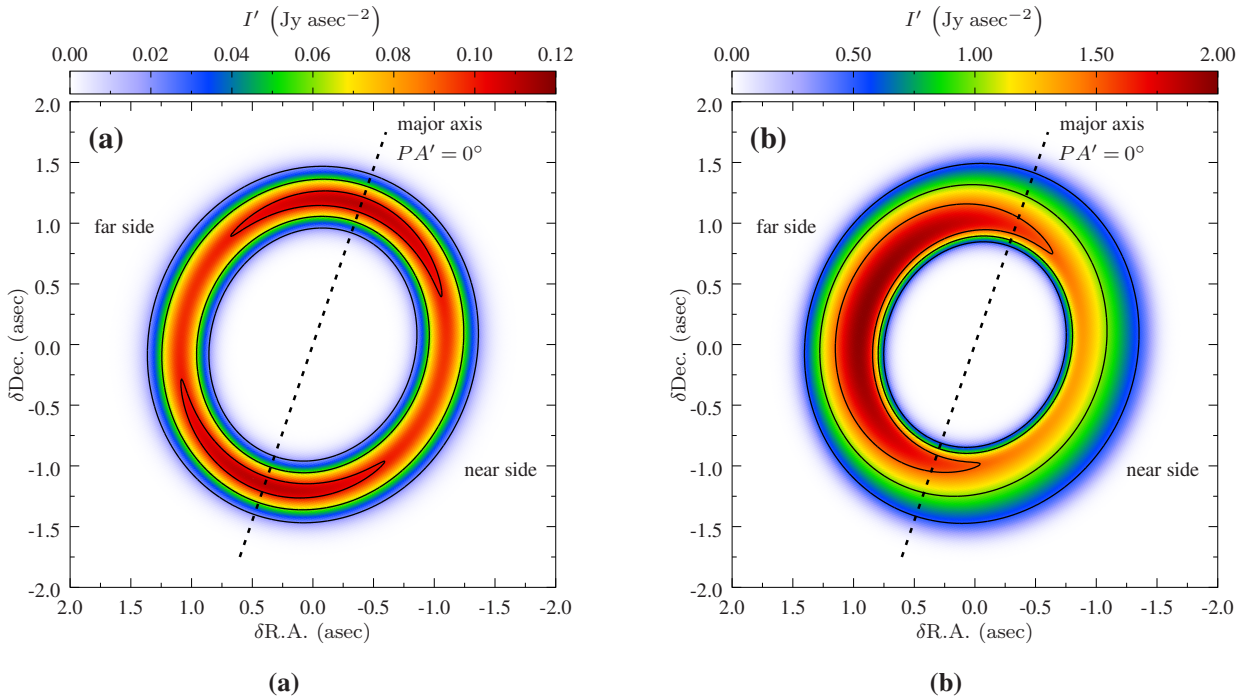


**Fig. 3:** Disk intensity images obtained by ray-tracing simulation.  $I'$  is the intensity before beam convolution. The dashed line indicates the major axis of the disk along  $PA' = 0^\circ$ . The simulated images are based on  $w_0 = 27$  au and  $r_0 = 175$  au models. **(a):**  $\Sigma_0 = 0.01$  g cm $^{-2}$  model. The contours are drawn at  $I' = 0.02, 0.06, 0.10$  Jy asec $^{-2}$ . **(b):**  $\Sigma_0 = 1.00$  g cm $^{-2}$  model. The contours are drawn at  $I' = 0.50, 1.00, 1.50$  Jy asec $^{-2}$ .

extended slightly when necessary.

2. Calculate the density  $\rho(r, z)$ , temperature  $T(r, z)$ , and mean intensity  $J_\nu(r, z)$  for each  $(\Sigma_0, w_0, r_0)$  by assuming the radiative and hydrostatic equilibria (Section 3.2).
3. Calculate model intensity by ray-tracing, and extract the radial profiles after convolving the image with the synthesized beam of the observation (Section 3.3).
4. Fit the radial profiles of the model intensity with the Gaussian function and obtain their  $(I_0^*, w_0^*, r_0^*)$  of the model, which are compared with  $(I_{0,\text{obs}}^*, w_{0,\text{obs}}^*, r_{0,\text{obs}}^*)$  in the same  $PA'$  sector (Section 3.4). Search for parameters  $(\Sigma_0, r_0, w_0)$  that meet the criteria in equation (11). If necessary, construct a refined model by interpolating  $\Sigma_0$  and  $r_0$ .

In the following, we explain the procedure in detail.

### 3.1 Assumptions on dust properties

We assume a dust grain in the disk to be a compact sphere composed of silicate, carbonaceous compounds, and water ice; their mass fractional abundances relative to the hydrogen mass are taken to be 0.0043, 0.0030, and 0.0094, respectively, which are consistent with the solar elemental abundance (Anders & Grevesse 1989). The grains have a power-law size distribution,

$$\frac{dn(a)}{da} \propto a^{-3.5}, \quad a_{\text{max}} = 1 \text{ mm}, \quad (3)$$

where  $a$  and  $a_{\text{max}}$  denote the grain radius and the maximum grain radius, respectively. The choice of  $a_{\text{max}}$  is based on the observed spectral opacity index,  $\beta \sim 1$  (Verhoeff et al. 2011). The absorption and scattering cross sections,  $C_a(a)$  and  $C_s(a)$ , and the asymmetry parameter  $g(a)$ <sup>1</sup> for every grain size in the power-law distribution are calculated using Mie theory. The scattering cross section and its asymmetry parameter are defined as

$$C_s(a) = \int_{4\pi} \frac{dC_s(a)}{d\Omega} d\Omega \quad (4)$$

and

$$g(a) = \frac{1}{C_s(a)} \int_{4\pi} \frac{dC_s(a)}{d\Omega} \cos \Theta(a) d\Omega, \quad (5)$$

respectively, where  $dC_s(a)/d\Omega$  is the differential scattering cross section and  $\Theta(a)$  the deflection angle from the propagation direction  $\Theta(a) = 0^\circ$ . To take into account the effects of asymmetric scattering in the M1 model (see Appendix 1 for more details), we incorporate the asymmetry parameter by multiplying  $C_s(a)$  by  $[1 - g(a)]$ ; the light scattered away from the propagation direction is treated

<sup>1</sup> The asymmetry parameter describes the anisotropy in scattering and takes value within  $|g| \leq 1$  (see, e.g., Bohren & Huffman 1983). For symmetric scattering about the axis perpendicular to the propagation direction of incident wave,  $g = 0$ . If the grain tends to scatter light toward the forward (backward) direction,  $g$  is positive (negative).

as extinction along  $\Theta = 0^\circ$ . In this way, the effects of self-scattering are considered while keeping the computational time for radiative transfer reasonable. Denoting the grain mass by  $m(a)$ , the scattering opacity used in this study is then defined as

$$\kappa_s = \int \left\{ \frac{C_s(a)}{m(a)} [1 - g(a)] \right\} \frac{dn(a)}{da} da, \quad (6)$$

which is weighted by the size distribution. Similarly, dividing  $C_a(a)$  by  $m(a)$  and integrate over the size distribution we obtain the absorption opacity as

$$\kappa_a = \int \left\{ \frac{C_a(a)}{m(a)} \right\} \frac{dn(a)}{da} da. \quad (7)$$

The opacities are shown in figure 2. When  $a_{\max}$  is comparable to  $\lambda_{\text{obs}}$ ,  $\kappa_s$  is larger than  $\kappa_a$  by a factor of about 10;  $\kappa_a = 2.9 \text{ cm}^2 \text{ g}^{-1}$  and  $\kappa_s = 26.2 \text{ cm}^2 \text{ g}^{-1}$  at  $\lambda_{\text{obs}} = 890 \text{ }\mu\text{m}$  (Aikawa & Nomura 2006). As will be described in Section 5.1, we also use model where  $\kappa_s$  is reduced by 90% from the conventional value.

### 3.2 Disk models

Applying the dust properties and the dust distribution, we solve the radiative transfer of the disk by the M1 model (González et al. 2007; Kanno et al. 2013; see also Appendix 1). The 2D distributions of the dust density  $\rho(r, z)$ , the temperature  $T(r, z)$ , and the mean intensity  $J_\nu(r, z)$  are determined by the same method as Muto et al. (2015). We consider the star as the heat source and use 226 colors in  $0.1 \text{ }\mu\text{m} \leq \lambda \leq 3.16 \text{ mm}$  (spectral resolution of  $\Delta \log \lambda = 0.02$ ) to calculate the radiative and hydrostatic equilibria. In the cylindrical coordinates  $(r, \varphi, z)$ , the star is located at the origin, while the disk is assumed to be axisymmetric around the  $z$ -axis and reflection symmetric with respect to the midplane ( $z = 0$ ). The computation region covers  $30 \text{ au} \leq r \leq 410 \text{ au}$  and  $0 \text{ au} \leq z \leq 120 \text{ au}$  with a spatial resolution of 2 au. We did not take the effects of accretion into account. We also did not consider the shadows cast by the inner warped disk discussed by Marino et al. (2015).

### 3.3 Model Image

The emergent intensity of the model is calculated by ray-tracing along the line of sight  $z'$ :

$$\frac{dI'}{dz'} = -(\kappa_a + \kappa_s)\rho(I' - S_\nu), \quad (8)$$

where the source function is given by

$$S_\nu = (1 - \eta) B_\nu(T) + \eta J_\nu. \quad (9)$$

The source function is the sum of the Planck function  $B_\nu(T)$  and the angular-averaged intensity  $J_\nu$ , each weighted by  $(1 - \eta)$  and  $\eta$ , where



$$\eta \equiv \frac{\kappa_s}{\kappa_a + \kappa_s}, \quad (10)$$

is the albedo. We obtain intensity distribution on the uniform grid of 2 au on the sky plane to construct the model image.

Figure 3 shows the intensity images obtained by ray-tracing for two peak surface density models,  $\Sigma_0 = 0.01 \text{ g cm}^{-2}$  and  $1.00 \text{ g cm}^{-2}$ , with  $w_0 = 27 \text{ au}$ ,  $r_0 = 175 \text{ au}$ , and  $i = 27^\circ$ . The former represents an optically thin disk, while the latter represents an optically thick disk. In the following, the coordinates of the disk projected in the sky are denoted by  $(r', PA')$ , i.e., coordinates with primes ( $'$ ). The regions of  $0^\circ < PA' < 180^\circ$  and  $180^\circ < PA' < 360^\circ$  correspond to the far side and the near side, respectively. The disk images appear slightly elongated in the major axis ( $PA' = 0^\circ$ ) because of the disk inclination, but they are reflection symmetry with respect to the minor axis ( $PA' = 90^\circ$ ). The intensity depends on  $PA'$  although the model is axisymmetric. It is highest on the major axis in the optically thin disk (figure 3a), but on the far side in the optically thick disk (figure 3b). When the disk is optically thin, the intensity is roughly proportional to the amount of dust along the line of sight. The major axis is brightest since the line of sight intersects the disk plane longer. When the disk is optically thick, the hot inner wall facing the star is exposed to us on the far side, thus its intensity is higher than that on the near side where the wall is hidden from sight. We take this  $PA'$  dependence into account in our analysis.

The next step is the convolution of the above images with a Gaussian beam to mimic the observation. Physical quantities obtained after beam convolution are indicated with asterisks (\*). Since the beam is elliptical with its major axis lying along  $PA' = 78.9^\circ$ , the image no longer retains its reflection symmetry with respect to the minor axis after the beam convolution. We then extract the radial intensity profiles from the convolved image and fit them with Gaussian function to obtain  $I_0^*$ ,  $w_0^*$ , and  $r_0^*$ .

### 3.4 Comparison between observation and simulation

For each sector, a parameter cube  $(I_0^*, w_0^*, r_0^*)$  associated with  $(\Sigma_0, w_0, r_0)$  is created. The best fit parameters for the dust distribution are searched by comparing the Gaussian-fitted values between the model and the observation. The best fit model should satisfy the following criteria:

$$|\Delta I_0^*| \equiv \left| I_{0,\text{obs}}^* - I_0^* \right| \leq 0.01 I_{0,\text{obs}}^*, \quad (11a)$$

$$|\Delta w_0^*| \equiv \left| w_{0,\text{obs}}^* - w_0^* \right| \leq 1 \text{ au}, \quad (11b)$$

$$|\Delta r_0^*| \equiv \left| r_{0,\text{obs}}^* - r_0^* \right| \leq 1 \text{ au}. \quad (11c)$$

In order to discern the trend in the  $PA'$  direction, criteria better than the beam resolution are set. These criteria are different from those of Muto et al. (2015), who placed a  $\pm 10\%$  tolerance for all the criteria above.

To facilitate the parameter search for the dust distribution and to save the computational time, we interpolate models to complement our sample on  $\Sigma_0$  and  $r_0$ . The interpolation among four adjacent  $(\Sigma_0, w_0, r_0)$  models at  $(r, z)$  is carried out by the following weighted average:

$$A(r, z; \Sigma_{0,i}, w_0, r_{0,i}) = \sum_{n=1}^2 l_n \left[ \sum_{m=1}^2 k_m A(r + r_{0,m} - r_{0,i}, z; \Sigma_{0,n}, w_0, r_{0,m}) \right], \quad (12)$$

where  $A$  represents  $\rho$ ,  $T$ , or  $J_\nu$ . The weighting factors  $f_m$  and  $g_n$  are defined as

$$\begin{aligned} k_1 &= 1 - \left| \frac{r_{0,i} - r_{0,1}}{r_{0,2} - r_{0,1}} \right| \\ k_2 &= 1 - k_1 \\ l_1 &= 1 - \left| \frac{\Sigma_{0,i} - \Sigma_{0,1}}{\Sigma_{0,2} - \Sigma_{0,1}} \right| \\ l_2 &= 1 - l_1 \end{aligned}$$

The subscripts “1” and “2” specify the two existing models, while the subscript “i” specifies the interpolated product. We do not perform interpolation on  $w_0$  because its 2-au interval in the parameter space is sufficiently refined to fulfill equation (11b).

## 4 Results

### 4.1 Derived best fit values

Figure 4 shows the results of the model fitting for all  $PA'$  sectors. The 15 radial profiles in  $PA' = 10^\circ - 310^\circ$  are well reproduced by the models; their parameters are listed in table 2. The mass contained in each  $PA'$  sector,  $M_{\text{sec}}$ , is also presented. However, none of the models succeed in reproducing the three radial profiles in  $PA' = 310^\circ - 10^\circ$  (figure 4d, 4e, and 4f). These three sectors will be described separately in Section 4.2.

We derived  $\Sigma_0 = 1.12 \text{ g cm}^{-2}$  for the brightest  $PA' = 30^\circ - 50^\circ$ , and  $\Sigma_0 = 8.31 \times 10^{-3} \text{ g cm}^{-2}$  for the faintest  $PA' = 230^\circ - 250^\circ$ . The contrast in  $\Sigma_0$  between these two sectors is about a factor of 130, which is twice the value derived by Muto et al. (2015). The apparent discrepancy is discussed in Section 4.3. Our model might overestimate the temperature in the north ( $PA' \approx 11^\circ$ ) and the south ( $PA' \approx 191^\circ$ ) of the outer disk, as we did not consider the possible shadowing effects caused by the warped inner disk (Marino et al. 2015; Casassus et al. 2015). As a consequence, the best fit  $\Sigma_0$  for  $PA' = 350^\circ - 10^\circ$  and  $PA' = 150^\circ - 170^\circ$  might be considered as lower limits.

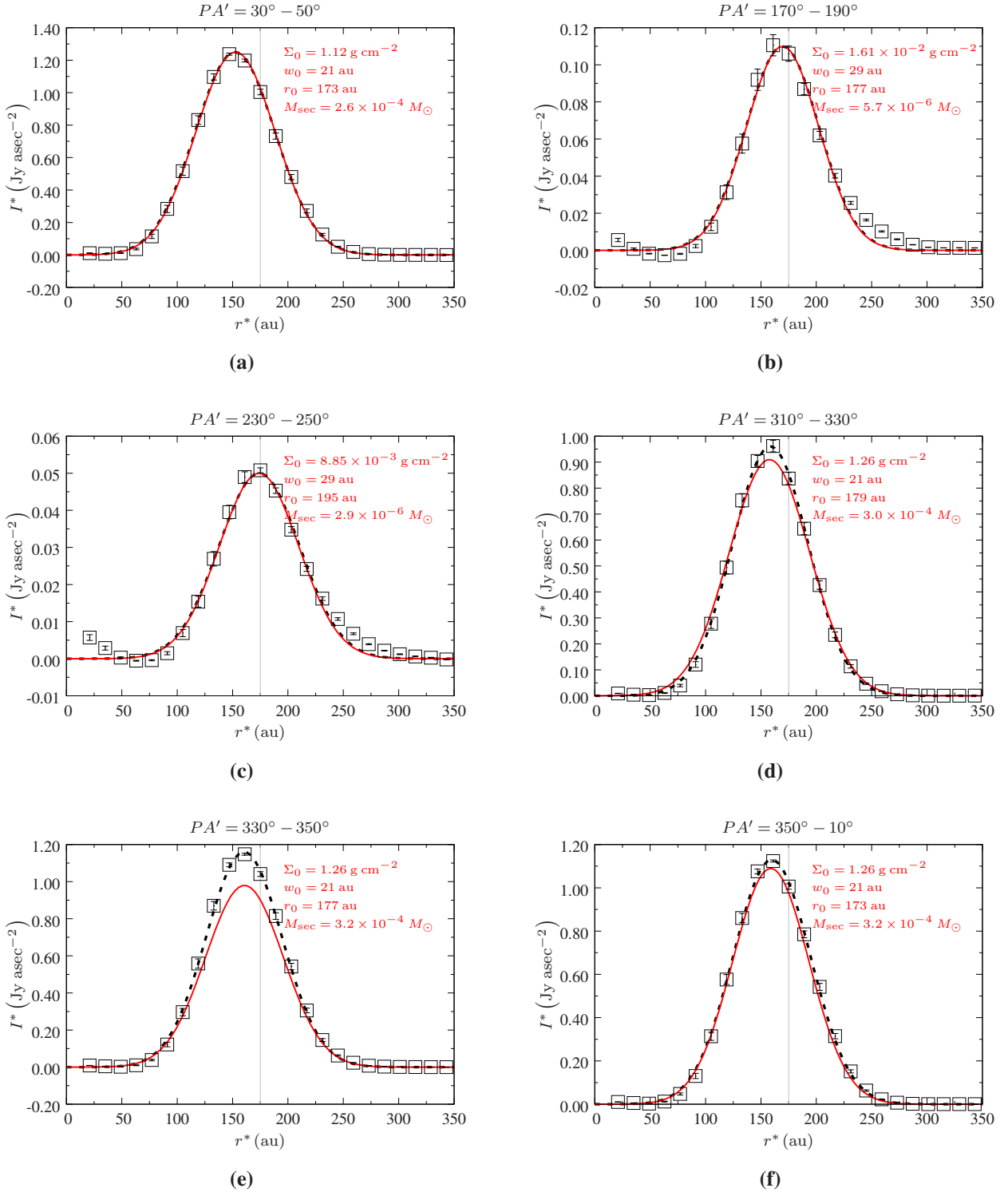


**Fig. 4:** The observed radial intensity profiles (plotted in square boxes with error bars in the  $I_{\text{obs}}^*$  direction) at  $\lambda_{\text{obs}} = 890 \mu\text{m}$  of six  $PA'$  sectors as examples. Black dashed lines are Gaussian-fitted curves for the observational data points. The faint gray line at  $r^* = 175$  au is drawn to emphasize the relative position of  $I_{0,\text{obs}}^*$  among the  $PA'$  sectors. Red solid lines are the modeling results using the conventional model for dust opacity. The best fit parameters and the disk mass of the sector are written on the top right in each plot. The modeling results for  $PA' = 310^\circ - 330^\circ$ ,  $PA' = 330^\circ - 350^\circ$ , and  $PA' = 350^\circ - 10^\circ$  do not meet the criteria in equation (11).

**Table 2:** Derived best fit values using the conventional model for dust opacity.

$PA'$	$\Sigma_0$ ( $\text{g cm}^{-2}$ )	$w_0$ (au)	$r_0$ (au)	$M_{\text{sec}}$ ( $M_{\odot}$ )	$\Delta I_0^*$ ( $\times I_{0,\text{obs}}^*$ )	$\Delta w_0^*$ (au)	$\Delta r_0^*$ (au)
$10^\circ - 30^\circ$	$7.89 \times 10^{-1}$	23	175	$2.1 \times 10^{-4}$	$-1.3 \times 10^{-5}$	+0.8	-0.5
$30^\circ - 50^\circ$	1.12	21	173	$2.6 \times 10^{-4}$	$-2.9 \times 10^{-5}$	+0.3	-0.3
$50^\circ - 70^\circ$	$7.28 \times 10^{-1}$	21	173	$1.5 \times 10^{-4}$	$-1.0 \times 10^{-5}$	-0.3	-0.5
$70^\circ - 90^\circ$	$3.07 \times 10^{-1}$	21	167	$5.9 \times 10^{-5}$	$-2.5 \times 10^{-5}$	+0.1	-0.3
$90^\circ - 110^\circ$	$2.00 \times 10^{-1}$	21	165	$3.8 \times 10^{-5}$	$-4.0 \times 10^{-5}$	-0.4	+0.8
$110^\circ - 130^\circ$	$1.33 \times 10^{-1}$	23	165	$2.7 \times 10^{-5}$	$-1.6 \times 10^{-5}$	-0.2	-0.1
$130^\circ - 150^\circ$	$7.83 \times 10^{-2}$	23	165	$1.9 \times 10^{-5}$	$-4.0 \times 10^{-5}$	+0.4	+0.6
$150^\circ - 170^\circ$	$3.61 \times 10^{-2}$	27	171	$1.1 \times 10^{-5}$	$-1.1 \times 10^{-5}$	+0.2	-0.8
$170^\circ - 190^\circ$	$1.61 \times 10^{-2}$	29	177	$5.7 \times 10^{-6}$	$-4.3 \times 10^{-5}$	+0.5	-0.0
$190^\circ - 210^\circ$	$1.10 \times 10^{-2}$	29	189	$4.1 \times 10^{-6}$	$-4.5 \times 10^{-5}$	+0.5	-0.6
$210^\circ - 230^\circ$	$9.05 \times 10^{-3}$	32	193	$3.5 \times 10^{-6}$	$-1.3 \times 10^{-5}$	-0.7	+0.7
$230^\circ - 250^\circ$	$8.31 \times 10^{-3}$	32	195	$3.0 \times 10^{-6}$	$-4.6 \times 10^{-5}$	-0.7	+0.8
$250^\circ - 270^\circ$	$2.89 \times 10^{-2}$	23	185	$6.8 \times 10^{-6}$	$-1.7 \times 10^{-5}$	-0.4	+0.1
$270^\circ - 290^\circ$	$8.60 \times 10^{-2}$	23	183	$2.0 \times 10^{-5}$	$-3.6 \times 10^{-5}$	+0.2	-0.0
$290^\circ - 310^\circ$	$2.21 \times 10^{-1}$	23	179	$4.9 \times 10^{-5}$	$-1.5 \times 10^{-5}$	+0.3	+0.1
* $310^\circ - 330^\circ$	1.26	21	179	$3.0 \times 10^{-4}$	( $-5.7 \times 10^{-2}$ )	(-2.9)	+0.9
* $330^\circ - 350^\circ$	1.26	21	177	$3.2 \times 10^{-4}$	( $-1.6 \times 10^{-1}$ )	(-1.2)	-0.4
* $350^\circ - 10^\circ$	1.26	21	173	$3.2 \times 10^{-4}$	( $-3.4 \times 10^{-2}$ )	+0.7	+1.0

\*  $PA' = 310^\circ - 330^\circ$ ,  $PA' = 330^\circ - 350^\circ$ , and  $PA' = 350^\circ - 10^\circ$  are failed to be reproduced using the conventional model. The parenthesized parameters are those that do not fulfill the criteria in equation (11).

#### 4.2 The northwest region of the disk

We encountered two difficulties in reproducing the three radial profiles in  $PA' = 310^\circ - 10^\circ$ . First, the model intensity is lower than the observed intensity even at  $\Sigma_0 = 1.26 \text{ g cm}^{-2}$ . In particular, it is 16% lower than  $I_{0,\text{obs}}^*$  in  $PA' = 330^\circ - 350^\circ$ . Second, the model profiles in  $PA' = 310^\circ - 350^\circ$  have larger radial extent than those observed even when the model width is set to be  $w_0 = 21 \text{ au}$ . The situation is shown more clearly in figure 5, where the model peak intensity  $I'_0$  is plotted as a function of  $\Sigma_0$  for three sectors,  $PA' = 80^\circ - 100^\circ$ ,  $350^\circ - 10^\circ$ , and  $260^\circ - 280^\circ$ ; they correspond to the far side, the major axis, and the near side, respectively. In  $\Sigma_0 < 0.1 \text{ g cm}^{-2}$ , the peak intensities are roughly proportional to  $\Sigma_0$  and are the same for the far and near sides since the disk is optically thin. This can

be confirmed in the model image shown in figure 3a. In  $\Sigma_0 > 0.1 \text{ g cm}^{-2}$ , the slope is shallower for a higher  $\Sigma_0$ , and  $I'_0$  reaches a ceiling. The ceiling of  $I'_0$  is highest on the far side, followed by the major axis, and last, on the near side (figure 3b).

The saturation of the peak intensity can be understood as follows. At  $\Sigma_0 \approx 0.1 \text{ g cm}^{-2}$ , the effective optical thickness defined as

$$\tau_{\text{eff}} \approx \Sigma_0 \sqrt{\kappa_a(\kappa_a + \kappa_s)} \quad (13)$$

is approximately unity, while the optical thickness by absorption only is  $\tau_a \approx 0.3$ . The effective optical thickness takes account of the diffusion length of a photon in the presence of scattering (Rybicki & Lightman 1979). When  $\tau_{\text{eff}}$  is less than unity, the medium is effectively thin or translucent. Hence, the intensity is roughly proportional to the column density along the line of sight when the medium is isothermal (see Fig. 8 in Muto et al. 2015 for the temperature distribution). When  $\Sigma_0 > 0.1 \text{ g cm}^{-2}$ , i.e.,  $\tau_{\text{eff}} > 1$ , the disk is opaque and the intensity reaches a ceiling. At the same time, the peak intensity depends on  $PA'$  for a given  $\Sigma_0$  model (figure 3b). The azimuthal dependence comes mainly from the difference in the temperature of the emitting surface, or the effective photosphere, which is discussed quantitatively in Section 5.2.

When  $\Sigma_0 > 1.0 \text{ g cm}^{-2}$ , the intensity profile is also significantly broadened in the radial direction because the intensity becomes insensitive to the increase in  $\Sigma_0$ , i.e., the profile becomes saturated even before the beam convolution (figure 3). This situation can also be seen in table 2, where we have chosen the maximum  $\Sigma_0$  so that the peak intensity is as high as possible in our parameter space. The width in the model image,  $w_0^*$ , is wider than the observed value,  $w_{\text{obs}}^*$ , by more than 6% in  $PA' = 310^\circ - 350^\circ$ . Therefore, we conclude that the dust opacity applied here cannot reproduce the radial intensity profiles in  $PA' = 310^\circ - 10^\circ$  due to the low intensity ceiling compared to the observation, as well as its associated effect of broadening the intensity profile.

#### 4.3 Uncertainties in the best fit values

The best fit values cannot be strictly constrained because of the insufficient angular resolution ( $\approx 60 \text{ au}$  in FWHM). Furthermore, in the optically thick region the intensity reaches a ceiling, resulting in even larger uncertainties in the results, especially in  $\Sigma_0$ . The uncertainties in the optically thin and optically thick sectors are discussed separately, by using the radial profiles of  $PA' = 30^\circ - 50^\circ$  and  $PA' = 230^\circ - 250^\circ$  as case studies. We investigate the dependence of  $M_{\text{sec}}$  on  $w_0$ , by treating  $\Sigma_0$  in equation (14) as the bound variable.

In the regime of optically thin and constant temperature,

$$I_0^* \propto \Sigma_0 w_0, \quad (14)$$

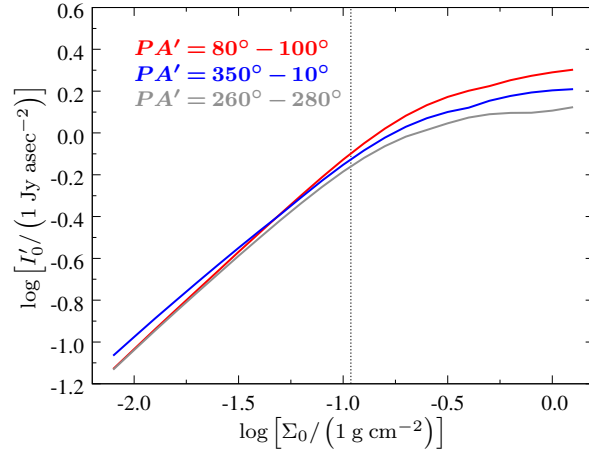


**Fig. 5:** The peak intensity  $I'_0$  achievable in  $PA' = 80^\circ - 100^\circ$  (the far side, red plots),  $PA' = 350^\circ - 10^\circ$  (the major axis, blue plots), and  $PA' = 260^\circ - 280^\circ$  (the near side, gray plots), regardless of  $r'$ . The  $I'_0$  values are values before beam convolution. In the analysis,  $w_0$  and  $r_0$  are fixed at 27 au and 175 au, respectively. The vertical, black dotted line denotes the  $\Sigma_0$  value where  $\tau_{\text{eff}} = 1$ .

**Table 3:** Fit values for  $PA^* = 230^\circ - 250^\circ$ .

Model parameters					Model results					
$\Sigma_0$	$w_0$	$r_0$	$\Sigma_0 w_0$	$M_{\text{sec}}$	$I_0^*$	$w_0^*$	$r_0^*$	$\Delta I_0^*$	$\Delta w_0^*$	$\Delta r_0^*$
( $\text{g cm}^{-2}$ )	(au)	(au)	( $\text{g cm}^{-2}$ au)	( $M_\odot$ )	( $\text{Jy asec}^{-2}$ )	(au)	(au)	( $\times I'_{0,\text{obs}}$ )	(au)	(au)
$8.31 \times 10^{-3}$	32	195	0.27	$3.0 \times 10^{-6}$	0.05	52.3	173.3	$4.6 \times 10^{-5}$	-0.7	0.8
$8.85 \times 10^{-3}$	29	195	0.26	$2.9 \times 10^{-6}$	0.05	50.8	173.9	$1.7 \times 10^{-5}$	0.8	0.3

**Table 4:** Fit values for  $PA' = 30^\circ - 50^\circ$ .

Model parameters					Model results					
$\Sigma_0$	$w_0$	$r_0$	$\Sigma_0 w_0$	$M_{\text{sec}}$	$I_0^*$	$w_0^*$	$r_0^*$	$\Delta I_0^*$	$\Delta w_0^*$	$\Delta r_0^*$
( $\text{g cm}^{-2}$ )	(au)	(au)	( $\text{g cm}^{-2}$ au)	( $M_\odot$ )	( $\text{Jy asec}^{-2}$ )	(au)	(au)	( $\times I'_{0,\text{obs}}$ )	(au)	(au)
1.12	21	173	23.52	$2.6 \times 10^{-5}$	1.25	50.7	152.6	$2.9 \times 10^{-5}$	0.3	-0.3
$8.99 \times 10^{-1}$	23	173	20.68	$2.3 \times 10^{-5}$	1.25	51.7	152.1	$1.8 \times 10^{-5}$	-0.7	0.2

i.e., the peak intensity is proportional to the product of  $\Sigma_0$  and  $w_0$ , or equivalently  $M_{\text{sec}}$ . Despite the difference in their  $w_0$  values, the two parameter sets listed in table 3 for  $PA' = 230^\circ - 250^\circ$  satisfy the criteria in equation (11). The two sets, each with  $w_0 = 32$  au and  $w_0 = 29$  au, estimate  $M_{\text{sec}}$  to be  $3.0 \times 10^{-6} M_\odot$  and  $2.9 \times 10^{-6} M_\odot$ , respectively. Both  $\Sigma_0$  and  $w_0$  contain  $\pm 10\%$  uncertainties due to the criteria tolerance in equation (11), but  $M_{\text{sec}}$  is uncertain only by approximately  $\pm 5\%$ . This is

because  $I_0^*$  is proportional to  $M_{\text{sec}}$  in these optically thin sectors.

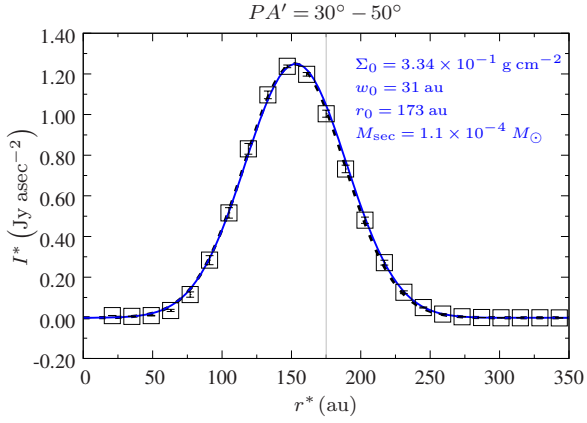
Similarly, in table 4 we listed two parameter sets for the optically thick  $PA' = 30^\circ - 50^\circ$ . The difference in terms of  $M_{\text{sec}}$  or  $\Sigma_0 w_0$  is about 11%, which is much larger than that for  $PA' = 230^\circ - 250^\circ$ . The difference in terms of  $w_0$  is about 10%, in contrast to the difference in  $\Sigma_0$  which reaches 20%. This implies that equation (14) breaks down when the intensity reaches a ceiling. Moreover, if we relax the criteria tolerance to follow Muto et al. (2015) (Section 3.4), a wider range of  $\Sigma_0 w_0$  can be obtained as best fit values, so as the uncertainties in the optically thick sectors (refer to Appendix 2 in Muto et al. 2015). This explains the discrepancy between our results and those derived by Muto et al. (2015): in this work the  $\Sigma_0$  value for  $PA' = 30^\circ - 50^\circ$  is about twice the value derived by Muto et al. (2015), resulting in the higher  $\Sigma_0$  contrast between  $PA' = 30^\circ - 50^\circ$  and  $PA' = 230^\circ - 250^\circ$ . The best fit results, especially the values of  $\Sigma_0$  in the optically thick region in  $PA' = 10^\circ - 130^\circ$  and  $PA' = 290^\circ - 310^\circ$ , contain uncertainties of a factor of  $\sim 2$ . Analysis based on observations with a higher angular resolution, or at a longer wavelength (thus less opaque in the emissions), should be able to better constrain  $\Sigma_0$  and  $w_0$ .

## 5 Discussions

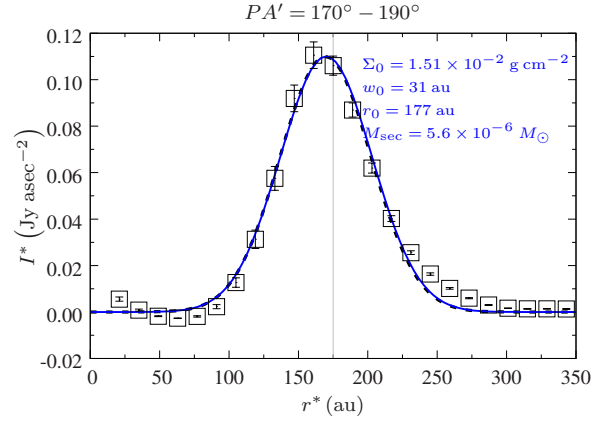
### 5.1 Reducing scattering opacities

Figure 5 shows that  $I'_0$  depends on both  $\Sigma_0$  and  $PA'$ , and it reaches a ceiling when  $\tau_{\text{eff}}$  exceeds unity. The low intensity ceiling is a consequence of the large scattering optical depth. Although the conventional properties of the dust grains are applied in the model, their actual opacity can be highly uncertain; they might be aggregates composed of monomers and have different composition (Tazaki et al. 2016), so that either the scattering cross section might have been overestimated or the asymmetry parameter been underestimated, or both. Therefore, as a tentative approach to reproduce the radial profiles in the northwestern region,  $PA' = 310^\circ - 10^\circ$ , we reduce the scattering opacity across all the wavelengths by 90%, as depicted in figure 2. The scattering opacity at  $\lambda_{\text{obs}}$  is then reduced to  $2.62 \text{ cm}^2 \text{ g}^{-1}$ , which approximates the absorption opacity. The purpose is to reduce the scattering optical depth, thus elevating the ceiling of  $I'_0$ . The absorption opacity of the dust particles is kept the same. Therefore the albedo  $\eta$  is thus effectively reduced. In the following, we denote this model by “reduced-scattering model”, in contrast to the “conventional model” which uses the conventional scattering opacity. We apply the reduced-scattering model to reproduce not only the radial profiles of the northwestern region, but also to all  $PA'$  sectors in order to study the relevant effects.

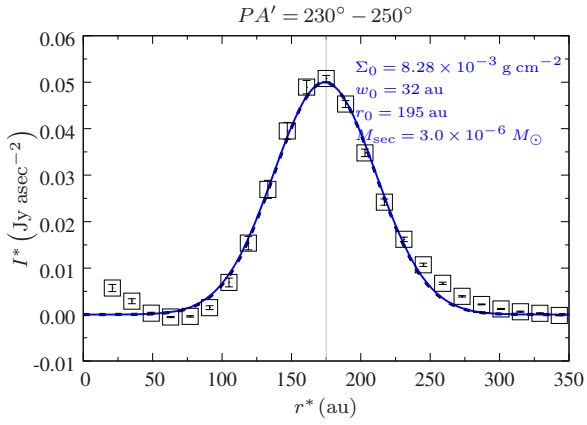
The results are shown in figure 6 and in table 5. We successfully reproduce the radial profiles in all sectors, including those in  $PA' = 310^\circ - 10^\circ$  (figure 6d, 6e, and 6f). In addition, the contrast in



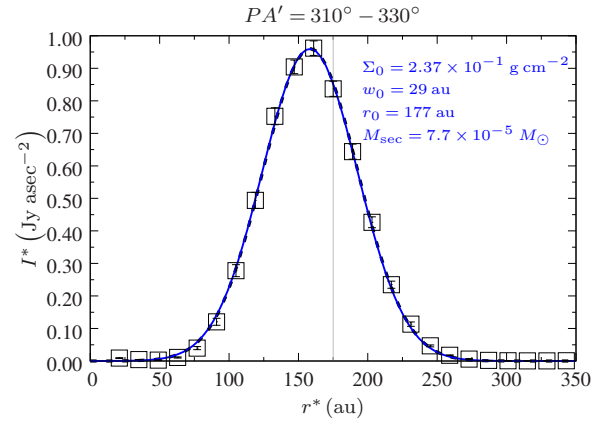
(a)



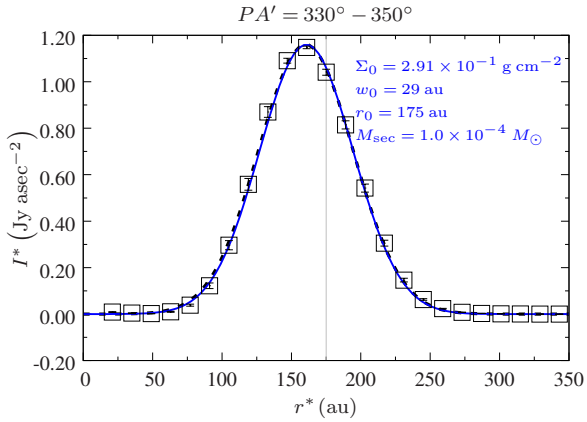
(b)



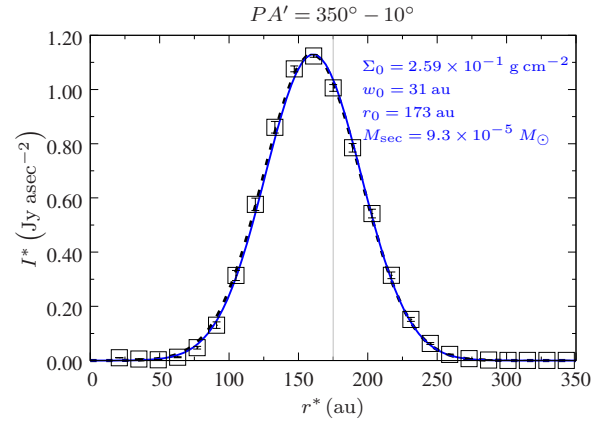
(c)



(d)



(e)



(f)

**Fig. 6:** Similar to figure 4, but the results (blue solid lines) here are derived by the reduced-scattering model. The radial profiles of  $PA' = 310^\circ - 330^\circ$ ,  $PA' = 330^\circ - 350^\circ$ , and  $PA' = 350^\circ - 10^\circ$  are well reproduced with the reduced-scattering model.



**Table 5:** Derived best fit values using the reduced-scattering model.

$PA'$	$\Sigma_0$ ( $\text{g cm}^{-2}$ )	$w_0$ (au)	$r_0$ (au)	$M_{\text{sec}}$ ( $M_{\odot}$ )	$\Delta I_0^*$ ( $\times I_{0,\text{obs}}^*$ )	$\Delta w_0^*$ (au)	$\Delta r_0^*$ (au)
$10^\circ - 30^\circ$	$2.76 \times 10^{-1}$	31	173	$1.0 \times 10^{-4}$	$-4.0 \times 10^{-5}$	+0.9	-0.0
$30^\circ - 50^\circ$	$3.34 \times 10^{-1}$	31	173	$1.1 \times 10^{-4}$	$-2.6 \times 10^{-5}$	-0.6	-0.9
$50^\circ - 70^\circ$	$3.33 \times 10^{-1}$	29	173	$9.8 \times 10^{-5}$	$-2.7 \times 10^{-5}$	-0.8	-0.5
$70^\circ - 90^\circ$	$2.46 \times 10^{-1}$	27	169	$6.1 \times 10^{-5}$	$-2.2 \times 10^{-5}$	-0.5	-0.6
$90^\circ - 110^\circ$	$1.84 \times 10^{-1}$	23	167	$3.9 \times 10^{-5}$	$-3.1 \times 10^{-5}$	+0.0	-0.9
$110^\circ - 130^\circ$	$1.24 \times 10^{-1}$	23	165	$2.8 \times 10^{-5}$	$-2.8 \times 10^{-5}$	+0.1	+0.2
$130^\circ - 150^\circ$	$6.94 \times 10^{-2}$	27	167	$2.0 \times 10^{-5}$	$-2.7 \times 10^{-5}$	-0.7	-0.7
$150^\circ - 170^\circ$	$3.32 \times 10^{-2}$	29	171	$1.1 \times 10^{-5}$	$-1.9 \times 10^{-5}$	-0.2	-0.9
$170^\circ - 190^\circ$	$1.51 \times 10^{-2}$	31	177	$5.7 \times 10^{-6}$	$-1.0 \times 10^{-5}$	-0.4	-0.5
$190^\circ - 210^\circ$	$1.07 \times 10^{-2}$	29	187	$3.9 \times 10^{-6}$	$-9.1 \times 10^{-6}$	+0.7	+0.6
$210^\circ - 230^\circ$	$8.97 \times 10^{-3}$	32	193	$3.5 \times 10^{-6}$	$-3.5 \times 10^{-5}$	-0.5	-0.2
$230^\circ - 250^\circ$	$8.28 \times 10^{-3}$	32	195	$3.0 \times 10^{-6}$	$-1.5 \times 10^{-5}$	-0.6	+0.1
$250^\circ - 270^\circ$	$2.80 \times 10^{-2}$	23	185	$6.5 \times 10^{-6}$	$-4.4 \times 10^{-5}$	+0.1	-0.3
$270^\circ - 290^\circ$	$7.26 \times 10^{-2}$	27	183	$2.0 \times 10^{-5}$	$-7.5 \times 10^{-7}$	-0.3	+0.9
$290^\circ - 310^\circ$	$1.46 \times 10^{-1}$	27	181	$4.2 \times 10^{-5}$	$-8.1 \times 10^{-7}$	-0.1	-0.6
$310^\circ - 330^\circ$	$2.37 \times 10^{-1}$	29	177	$7.7 \times 10^{-5}$	$-1.1 \times 10^{-5}$	+0.0	+0.3
$330^\circ - 350^\circ$	$2.91 \times 10^{-1}$	29	175	$1.0 \times 10^{-4}$	$-2.2 \times 10^{-5}$	+0.7	-0.4
$350^\circ - 10^\circ$	$2.59 \times 10^{-1}$	31	173	$9.6 \times 10^{-5}$	$-2.2 \times 10^{-5}$	+0.6	-0.9

$\Sigma_0$  between  $PA' = 30^\circ - 50^\circ$  and  $PA' = 230^\circ - 250^\circ$  is reduced to about a factor of 40, which is closer to the contrast in observed intensity. Using the reduced-scattering model, we plot  $I'_0$  as a function of  $\Sigma_0$  in figure 7. The results are essentially similar to those of the conventional model, but  $I'_0$  reaches a ceiling only at  $\Sigma_0 \approx 0.25 \text{ g cm}^{-2}$ , at which  $\tau_{\text{eff}} \approx 1$ . Besides, the reduced-scattering model is brighter than the conventional model in all the cases, especially when  $\Sigma_0$  exceeds  $0.1 \text{ g cm}^{-2}$ , where  $\tau_{\text{eff}}$  is approximately 1 in the conventional model but only 0.3 in the reduced-scattering model.

We summarize the best fit parameters and the dust masses derived from the conventional and the reduced-scattering models in figure 8. Compared to the conventional model, the reduced-scattering model estimates smaller  $\Sigma_0$  but larger  $w_0$  in the northern region. Furthermore, the  $\Sigma_0$  distribution in  $PA' = 310^\circ - 70^\circ$  is about  $0.3 \text{ g cm}^{-2}$  on average, contrary to the conventional model which derives about  $0.9 \text{ g cm}^{-2}$  for sectors in  $PA' = 10^\circ - 70^\circ$ . When scattering is dominant, the disk

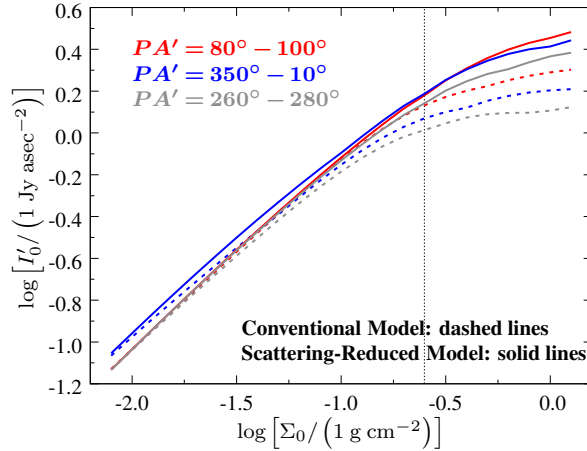


**Fig. 7:** The maximum surface brightness  $I'_0$  achievable in  $PA' = 80^\circ - 100^\circ$  (red plots),  $PA' = 350^\circ - 10^\circ$  (blue plots), and  $PA' = 260^\circ - 280^\circ$  (gray plots), regardless of  $r'$ . Solid and dashed lines are the results using the reduced-scattering and conventional models, respectively. The  $I'_0$  values are values before beam convolution. The vertical, black dotted line denotes the  $\Sigma_0$  value where  $\tau_{\text{eff}} = 1$  in the reduced-scattering model.

appearance is faint and indistinct, restricting only the model of small  $w_0$  and large  $\Sigma_0$  to reproduce  $w_{0,\text{obs}}^*$ . Reducing the scattering opacities sharpens the disk outline and thus allows us to reproduce the same  $I_0^*$  with a larger  $w_0$  but at a smaller  $\Sigma_0$ , as predicted by equation (14). Since the reduced-scattering model is yet to be optically thick for the intensity to reach a ceiling, it estimates about half the mass derived from the conventional model. The sectors within  $PA' = 130^\circ - 290^\circ$  show no significant changes in their best fit parameters like those in the northern region; their  $\tau_{\text{eff}}$  values are below unity so that the intensity is not much different between the conventional and reduced-scattering models. As a conclusion, reducing scattering opacity alters the results only in the optically thick northern sectors.

## 5.2 Intensity Dependence on Scattering Opacity and $PA'$

In this subsection we discuss why the reduced-scattering model can reproduce the ALMA observation while the conventional model cannot. We also discuss the origin of the azimuthal dependence of the peak intensity. For these purposes, we evaluate the model intensity quantitatively.

The solution of equation (8) is expressed as

$$I'(r; PA') = (\kappa_a + \kappa_s) \int_{-\infty}^{+\infty} \rho(r, z) S_\nu(r, z) e^{-\tau'} dz', \quad (15)$$

where  $\tau'$  denotes the optical depth measured from the observer to the point  $(r, z)$  in the disk along the line of sight  $z'$ , defined by

$$\tau'(r, z; PA') = (\kappa_a + \kappa_s) \int_{+\infty}^z \rho dz'. \quad (16)$$

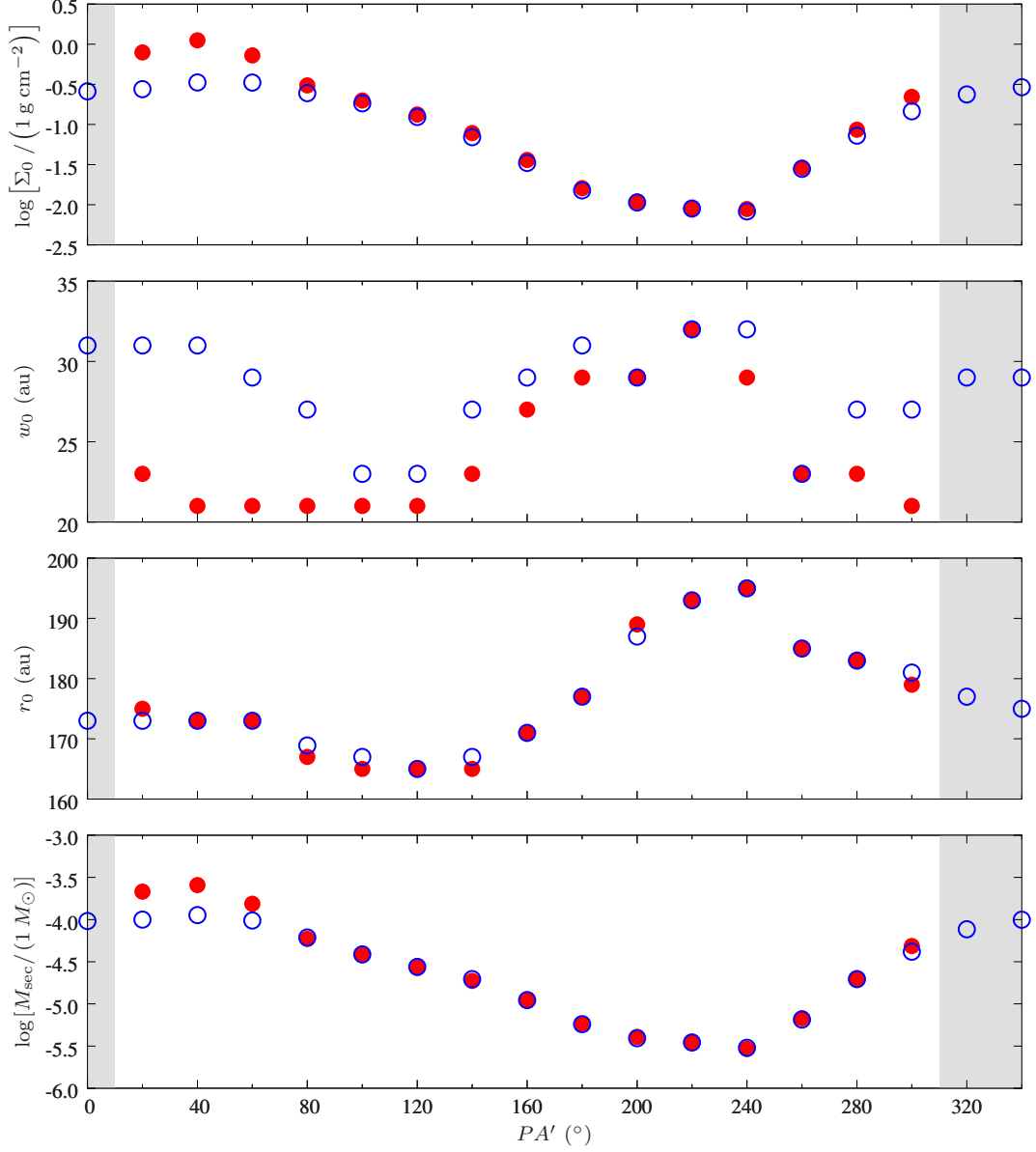


**Fig. 8:** The best fit parameters,  $\Sigma_0$ ,  $w_0$ ,  $r_0$ , and  $M_{\text{sec}}$ , distributions along the  $PA'$  direction, derived using the conventional (red filled circles) and the reduced-scattering model (blue open circles). The gray shaded portions indicate the  $PA'$  sectors where the radial profiles cannot be reproduced by the conventional model.

The observer is located at  $z = +\infty$ . The observable photon density,  $(\kappa_a + \kappa_s)\rho S_\nu \exp(-\tau')$ , denotes the emissivity per unit length in which absorption and scattering are taken into account by the attenuation factor  $\exp(-\tau')$ . Figure 9 shows the observable photon density in unit of  $\text{Jy asec}^{-2} \text{ au}^{-1}$  for the model of  $\Sigma_0 = 1.00 \text{ g cm}^{-2}$ ,  $w_0 = 27 \text{ au}$ , and  $r_0 = 175 \text{ au}$ . The left and right panels are based on the conventional and the reduced-scattering models, respectively. From top to bottom, the line of sight is offset from the  $z$ -axis by  $\theta = -27^\circ$ ,  $0^\circ$ , and  $+27^\circ$ . Since the inclination of the disk is  $i = 27^\circ$ , the top

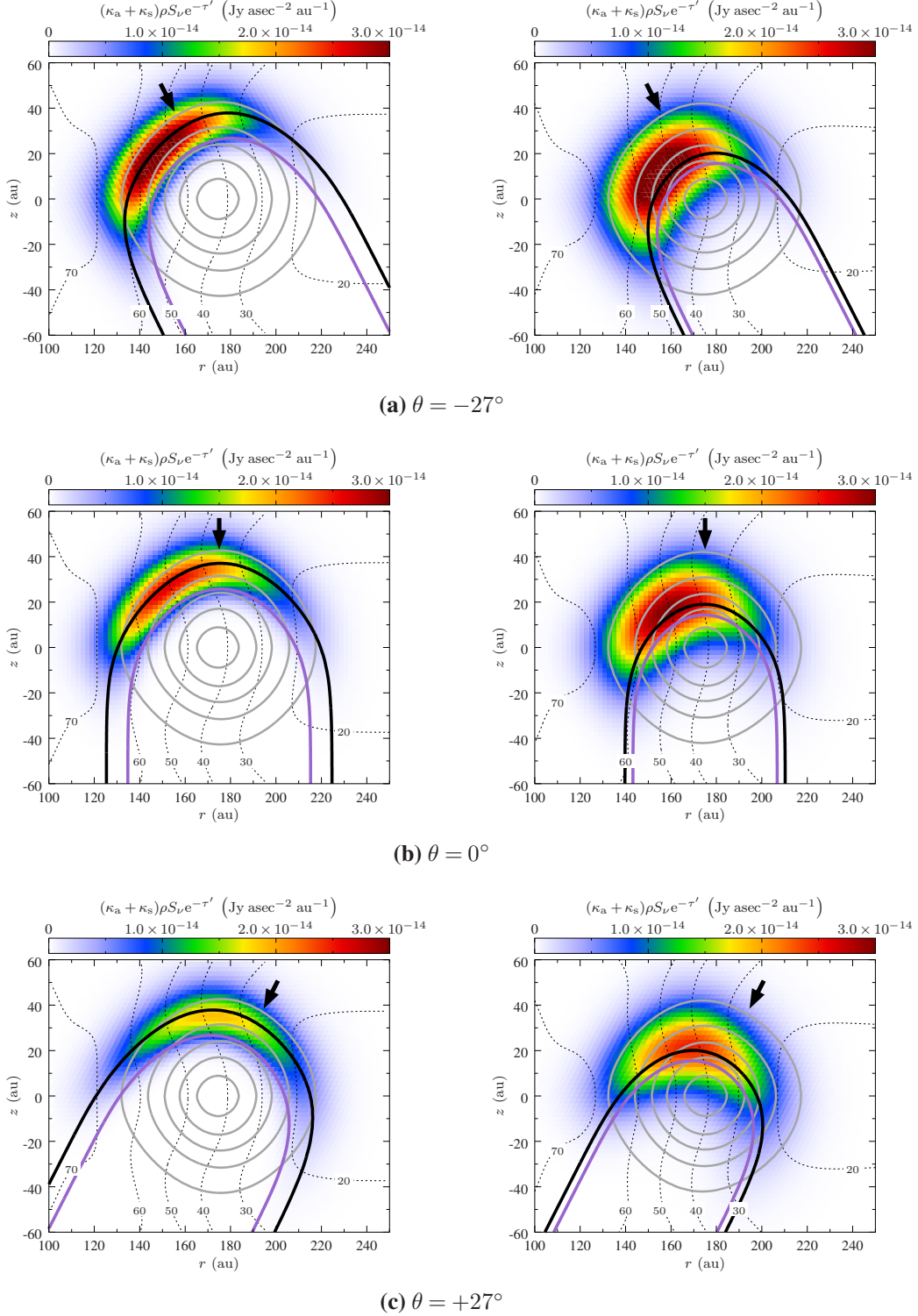


**Fig. 9:** The  $(\kappa_a + \kappa_s)\rho S_\nu \exp(-\tau')$  distributions of the conventional (left panels) and the reduced-scattering model (right panels), at a common  $\Sigma_0 = 1.00 \text{ g cm}^{-2}$ . The color scale is common for each panel. The top, middle, and bottom panels are the distributions at viewing angle  $\theta = -27^\circ$ ,  $0^\circ$ , and  $+27^\circ$ , respectively, as indicated by the black arrows. The black dotted contours are the temperature (units in K). The gray solid contours are the densities drawn at  $\rho(r, z) = 0.1, 0.3, 0.5, 0.7, 0.9$  of  $\rho_0(175 \text{ au}, 0 \text{ au}) = 1.3 \times 10^{-15} \text{ g cm}^{-3}$ , the peak density in the model. The surface where  $\tau' = 1$  and  $\tau_{\text{eff}} = 1$  are indicated by the thick black and the purple curves, respectively.

panels correspond to  $PA' = 90^\circ$  (the far side) while the bottom panels to  $PA' = 270^\circ$  (the near side). The middle panels where  $\theta = 0^\circ$  shows the observable photon density of a face-on disk; they do not actually correspond to  $PA' = 0^\circ$  because our line of sight does not lie in the  $(r, z)$  plane. However, the results can be regarded as a good substitute for the  $PA' = 0^\circ$  case since the inclination angle is small.

In each panel of figure 9, the gray solid and black dotted contours denote the density and temperature, respectively. The density and temperature are almost unchanged by the reduction of scattering. The observable photon density, on the other hand, is greatly different between the conventional and the scattering-reduced models, and it also varies with  $\theta$ . The thick black and purple curves denote the location of  $\tau' = 1$  and  $\tau_{\text{eff}} = 1$ , respectively; the location of  $\tau_{\text{eff}} = 1$  is plotted by scaling  $\tau'$  by a factor of  $(1 - \eta)^{-1/2}$ .

The observed photons come mainly from the region of  $\tau' = 1$ , where  $\tau_{\text{eff}}$  is still smaller than unity. This is because while most of the photons are often emitted from the  $\tau_{\text{eff}} = 1$  surface, the observed photons are scattered around  $\tau' = 1$  surface before reaching the observer. In the conventional model, the difference between  $\tau_{\text{eff}} = 1$  and  $\tau' = 1$  is large, and its observable photon emitting area is confined in a narrow region near  $\tau' = 1$  (left panels in figure 9). When the reduced-scattering model is applied, the regions of  $\tau_{\text{eff}} = 1$  and  $\tau' = 1$  become closer and the observable photon density extends over a wider area (right panels in figure 9). The narrowing of the emitting area in the conventional model is equivalent to the decrease in propagation speed of the photons caused by the dominant scattering. Considering that the source function of radiation is similar in both models, the intensity is higher in the reduced-scattering model because the line of sight crosses a longer path in the area of high observable photon density. It should be noted that the model peak intensity is lower than that of the blackbody radiation for the dust temperature in the presence of scattering.

The effects of scattering on the intensity is serious only when  $\kappa_s > \kappa_a$ . Further reduction in the scattering opacity will increase the intensity only by a little, thus we cannot set a lower limit on the scattering opacity from our modeling. Nevertheless, the scattering opacity of the dust grains should be appreciable since the pattern of polarization in the disk at  $\lambda = 890 \mu\text{m}$ , recently revealed by ALMA, seems consistent with the case of self-scattering (Kataoka et al. 2015; Kataoka et al. 2016).

The peak intensity shows azimuthal dependence when the disk is inclined, and the observed intensity strongly depends on the temperature of the effective photosphere when  $\tau'$  (or  $\tau_{\text{eff}}$ ) exceeds unity (figure 3b). The observable photon density at a given point depends on  $\theta$  through the attenuation factor  $\exp(-\tau')$ , and the peak density decreases in the order of which  $\theta = -27^\circ, 0^\circ$ , and  $+27^\circ$ . Since the temperature gradient is due to the heating from the central star, the decrease in the observable photon density directly corresponds to the decrease in the temperature of the effective photosphere

that we can observe. This is the origin of the azimuthal dependence shown in figures 3b and 5 when  $\tau_{\text{eff}} > 1$ , in which the far side is the highest in intensity while the near side is the lowest.

As mentioned at the beginning of Section 3, our 2D axisymmetric model might not be able to describe the scattered light properly in the crescent disk, especially when scattering is dominant. We discuss the validity of the axisymmetric disk by using figure 9. In the figure, the difference between  $\tau' = 1$  and  $\tau_{\text{eff}} = 1$  corresponds to the typical length travelled by a photon before escaping from the disk. Even when the albedo is high as in the conventional model, this length is approximately 10 au, much shorter than the arc length subtended by the  $20^\circ$ -sector at  $r_{0,\text{obs}}^* \approx 160$  au which is approximately 56 au. This implies that the contribution of scattered radiation from other sectors is negligible, and the 2D axisymmetric model is a good approximation to reproduce the asymmetry intensity distribution of the disk.

## 6 Summary

We derived the dust distribution in the crescent disk around HD 142527 by reproducing the observed radial intensity profiles of the continuum emission at  $890 \mu\text{m}$  obtained by ALMA Cycle 0. The radial distribution of surface density is assumed to be a Gaussian function whose peak and radial width are denoted as  $\Sigma_0$  and  $w_0$ , respectively. The radiative and hydrostatic equilibria in the disk are solved by radiative transfer calculations. We summarize our results as follows:

1. We first adopt the absorption opacity  $\kappa_a$  and scattering opacity  $\kappa_s$  as those of the compact spheres having composition consistent with the solar elemental abundance and a power-law size distribution with the maximum radius of 1 mm. At the modeling wavelength  $890 \mu\text{m}$ ,  $\kappa_s$  is about 10 times larger than  $\kappa_a$ . Using these conventional opacities, we cannot reproduce the radial intensity profiles in the northwestern region of the disk, observation of which shows high intensity and is located in the near side of the disk. The model intensity in this region reaches a lower ceiling than the observed peak intensity due to heavy scattering.
2. When the scattering opacity is reduced to 10% from the conventional value, the observed intensity distributions are reproduced successfully in all the position angles, including those in the northwestern region. The best fit values depend little on the scattering opacity in the southern region where the disk is optically thin. On the other hand,  $\Sigma_0$  is derived to be  $\sim 50\%$  smaller, while  $w_0$  becomes  $\sim 50\%$  wider in the optically thick northern region. The contrast in  $\Sigma_0$  between  $PA = 11^\circ - 31^\circ$  and  $PA = 211^\circ - 231^\circ$ , the brightest and the faintest regions in the dust continuum emission, is derived to be  $\approx 40$ , much smaller than the value for the cases of conventional opacities (70 – 130).

3. Detailed inspection of our model shows that in the case of inclined, optically thick disk, the temperature on the emitting surface depends on the position angle even when the disk is axisymmetric. As a result, the emergent peak intensity also varies azimuthally. By reducing the scattering opacity, we derived smaller  $\Sigma_0$  to reproduce the observed intensity in the northern region. This is not only because the location of emitting surface gets deeper into the disk, but also the portion of the disk that contributes to the observed intensity becomes larger.

## 7 Funding

This work is supported by MEXT KAKENHI Nos. 23103004, 24103504, and 26103702.

## 8 Acknowledgments

We thank Hideko Nomura for providing us the dust opacity used in this paper. We also thank Satoshi Okuzumi and Akimasa Kataoka for their valuable comments. This paper makes use of the following ALMA data: ADS/JAO.ALMA#2011.0.00318.S. ALMA is a partnership of ESO (representing its member states), NSF (USA) and NINS (Japan), together with NRC (Canada), NSC and ASIAA (Taiwan), and KASI (Republic of Korea), in cooperation with the Republic of Chile. The Joint ALMA Observatory is operated by ESO, AUI/NRAO and NAOJ. A part of data analysis was carried out on common use data analysis computer system at the Astronomy Data Center of NAOJ. K.L. Soon is supported by Japanese Government Scholarship.

## Appendix 1 The M1 model

Here, we summarize the M1 model, the approximation method used to solve the radiation transfer in our disk model (González et al. 2007). At coordinate  $\mathbf{x}$  and at time  $t$ , the radiation transfer equation for the specific intensity  $I_\nu(\mathbf{x}, t; \mathbf{n})$  along direction  $\mathbf{n}$  is

$$\begin{aligned} \frac{1}{c} \frac{\partial I_\nu(\mathbf{x}, t; \mathbf{n})}{\partial t} + \mathbf{n} \cdot \nabla I_\nu(\mathbf{x}, t; \mathbf{n}) = \\ \kappa_a \rho(\mathbf{x}, t) B_\nu(\mathbf{x}, t) - (\kappa_a + \kappa_s) \rho(\mathbf{x}, t) I_\nu(\mathbf{x}, t; \mathbf{n}) \\ + \kappa_s \rho(\mathbf{x}, t) \int_{4\pi} I_\nu(\mathbf{x}, t; \mathbf{n}') d\mathbf{n}', \end{aligned} \quad (\text{A1})$$

where  $\kappa_a$  and  $\kappa_s$  denote the absorption and scattering opacities at frequency  $\nu$ , respectively, while  $c$  and  $\rho$  the speed of light and the matter density. On the right hand side of the equation, the first term states that the emissivity of matter is proportional to the blackbody radiation  $B_\nu$  at temperature  $T$ , while the second term is read as the extinction by the matter. The last term, on the other hand, represents the intensity scattered from  $\mathbf{n}'$  into  $\mathbf{n}$ . In the M1 model, anisotropic scattering can be

accounted for by incorporating the factor  $(1 - g)$  in the scattering cross section  $C_s$  (see Section 3.1). Integrating equation (A1) and the dot product of equation (A1) between  $\mathbf{n}$  over solid angle yields

$$\frac{\partial E_\nu}{\partial t} + \nabla \cdot \mathbf{F}_\nu = \kappa_a \rho (4\pi B_\nu - cE_\nu), \quad (\text{A2})$$

$$\frac{\partial \mathbf{F}_\nu}{\partial t} + c^2 \nabla \cdot \mathcal{P}_\nu = -(\kappa_a + \kappa_s) c \rho \mathbf{F}_\nu, \quad (\text{A3})$$

respectively, where,  $E_\nu$ ,  $\mathbf{F}_\nu$ , and  $\mathcal{P}_\nu$  are defined as follows:

$$\begin{aligned} E_\nu &= \int_{4\pi} I_\nu(\mathbf{x}, t; \mathbf{n}) d\mathbf{n}, \\ \mathbf{F}_\nu &= \int_{4\pi} \mathbf{n} I_\nu(\mathbf{x}, t; \mathbf{n}) d\mathbf{n}, \\ \mathcal{P}_\nu &= \int_{4\pi} \mathbf{n} \mathbf{n} I_\nu(\mathbf{x}, t; \mathbf{n}) d\mathbf{n}, \end{aligned}$$

i.e., they are the zeroth, the first, and the second angular moments of the intensity, respectively. In writing the conservation equations (A2) and (A3), we assume coherent scattering whereby the last term on the right hand side of equation (A1) vanishes. The two conservation equations are closed by relating  $\mathcal{P}_\nu$  and  $E_\nu$  via

$$\mathcal{P}_\nu = \left( \frac{1 - \chi_\nu}{2} \mathcal{I} + \frac{3\chi_\nu - 1}{2} \frac{\mathbf{f}_\nu \mathbf{f}_\nu}{|\mathbf{f}_\nu|^2} \right) E_\nu, \quad (\text{A4})$$

where

$$\begin{aligned} \chi_\nu &= \frac{3 + 4|\mathbf{f}_\nu|^2}{5 + \sqrt{4 - 3|\mathbf{f}_\nu|^2}}, \\ \mathbf{f}_\nu &\equiv \frac{\mathbf{F}_\nu}{cE_\nu}, \end{aligned}$$

and  $\mathcal{I}$  the identity matrix.

As described in Section 3.2, we use the cylindrical coordinates  $(r, \varphi, z)$  in which the disk midplane coincides with  $z = 0$  and the star locates at the origin. The disk is symmetric around  $z$ -axis and with respect to the midplane. We consider the star as the heat source for the disk, and use 226 colors within  $0.1 \mu\text{m} \leq \lambda \leq 3.16 \text{ mm}$  (equivalent spectral resolution of  $\Delta \log \lambda = 0.02$ ) in the calculation. Decomposing the radiation energy density and the flux into the components each from the star and the disk (Kanno et al. 2013), we write

$$E_\nu(r, z) = E_{\nu, \text{star}}(r, z) + E_{\nu, \text{disk}}(r, z), \quad (\text{A5})$$

$$\mathbf{F}_\nu(r, z) = \mathbf{F}_{\nu, \text{star}}(r, z) + \mathbf{F}_{\nu, \text{disk}}(r, z). \quad (\text{A6})$$

The star is assumed to be a blackbody of effective temperature  $T_{\text{eff}}$ , and its radiation energy density and flux intercepted by the disk at  $(r, z)$  are evaluated as

$$E_{\nu, \text{star}}(r, z) = \frac{\pi R_{\text{star}}^2}{c(r^2 + z^2)} B_\nu(T_{\text{eff}}) \exp[-\tau(r, z)], \quad (\text{A7})$$



$$\mathbf{F}_{\nu,\text{star}}(r, z) = \frac{c}{\sqrt{r^2 + z^2}} \begin{pmatrix} r \\ z \end{pmatrix} E_{\nu,\text{star}}(r, z), \quad (\text{A8})$$

where  $\tau$  is defined as

$$\tau(r, z) = \int_0^r (\kappa_a + \kappa_s) \rho \left( r', \frac{zr'}{r} \right) \sqrt{1 + \left( \frac{z}{r} \right)^2} dr'. \quad (\text{A9})$$

The conservation equations in the disk then read

$$\frac{\partial E_{\nu,\text{disk}}}{\partial t} + \nabla \cdot \mathbf{F}_{\nu,\text{disk}} = \kappa_a \rho [4\pi B_\nu(T) - cE_{\nu,\text{disk}}] + \kappa_s \rho c E_{\nu,\text{star}}, \quad (\text{A10})$$

$$\frac{\partial \mathbf{F}_{\nu,\text{disk}}}{\partial t} + c^2 \nabla \cdot \mathcal{P}_{\nu,\text{disk}} = -(\kappa_a + \kappa_s) \rho c \mathbf{F}_{\nu,\text{disk}}. \quad (\text{A11})$$

Assuming the disk to be a static structure, the time evolution term for both  $E_{\nu,\text{disk}}$  and  $\mathbf{F}_{\nu,\text{disk}}$  equal zero. The mean intensity  $J_\nu$  is defined as

$$J_\nu = \frac{cE_\nu}{4\pi}, \quad (\text{A12})$$

which is consistent with equation (9).

The radiative transfer and hydrostatic equilibrium are calculated in tandem to obtain self-consistent  $\rho$ ,  $T$ , and  $J_\nu$  distributions in the disk. The dust temperature  $T$  at each location  $(r, z)$  satisfies the condition for thermal equilibrium,

$$\int \kappa_a [E_\nu - 4\pi B_\nu(T)] d\nu = 0. \quad (\text{A13})$$

Following Muto et al. (2015), we assume that the gas and dust are well mixed in the vertical direction and use the constant gas-to-dust ratio of 100 throughout the disk. The vertical density distribution of the disk is in equilibrium between the gas pressure gradient and the  $z$ -component of the star gravity,

$$\frac{dP}{dz} = \frac{GM_{\text{star}}z}{(r^2 + z^2)^{3/2}} \rho_{\text{gas}}, \quad (\text{A14})$$

where  $G$ ,  $M_{\text{star}}$ , and  $\rho_{\text{gas}}$  denote the gravitational constant, the mass of the star, and the density of the gas, respectively. The gas pressure  $P$  follows

$$P = \frac{k_B}{\mu m_H} \rho_{\text{gas}} T, \quad (\text{A15})$$

where  $k_B$  denotes the Boltzmann constant and  $m_H$  the mass of hydrogen atom. The mean molecular weight is assumed to be  $\mu = 2.339$ .

## References

Aikawa, Y., & Nomura, H. 2006, ApJ, 642, 1152

Anders, E., & Grevesse, N. 1989, *Geochim. Cosmochim. Acta*, 53, 197

Andrews, S. M., Wilner, D. J., Espaillat, C., et al. 2011, *ApJ*, 732, 42

Baruteau, C., & Zhu, Z. 2016, *MNRAS*, 458, 3927

Biller, B., Lacour, S., Juhász, A., et al. 2012, *ApJL*, 753, L38

Birnstiel, T., Dullemond, C. P., & Pinilla, P. 2013, *A&A*, 550, L8

Bohren, C. F., & Huffman, D. R. 1983, *Absorption and Scattering of Light by Small Particles* (New York: Wiley)

Brown, J. M., Blake, G. A., Qi, C., et al. 2009, *ApJ*, 704, 496

Calvet, N., D'Alessio, P., Hartmann, L., et al. 2002, *ApJ*, 568, 1008

Calvet, N., D'Alessio, P., Watson, D. M., et al. 2005, *ApJL*, 630, L185

Casassus, S., van der Plas, G., M, S. P., et al. 2013, *Nature*, 493, 191

Casassus, S., Wright, C. M., Marino, S., et al. 2015, *ApJ*, 812, 126

Chiang, E. I., & Goldreich, P. 1997, *ApJ*, 490, 368

Close, L. M., Follette, K. B., Males, J. R., et al. 2014, *ApJL*, 781, L30

Espaillat, C., Muzerolle, J., Najita, J., et al. 2014, *Protostars and Planets VI*, 497

Fujiwara, H., Honda, M., Kataza, H., et al. 2006, *ApJL*, 644, L133

Fukagawa, M., Tamura, M., Itoh, Y., et al. 2006, *ApJL*, 636, L153

Fukagawa, M., Tsukagoshi, T., Momose, M., et al. 2013, *PASJ*, 65, L14

Grady, C., Fukagawa, M., Maruta, Y., et al. 2015, *Ap&SS*, 355, 253

González, M., Audit, E., & Huynh, P. 2007, *A&A*, 464, 429

Isella, A., Pérez, L. M., Carpenter, J. M., et al. 2013, *ApJ*, 775, 30

Kanno, Y., Harada, T., & Hanawa, T. 2013, *PASJ*, 65, 72

Kataoka, A., Muto, T., Momose, M., et al. 2015, *ApJ*, 809, 78

Kataoka, A., Tsukagoshi, T., Momose, M., et al. 2016, *ApJL*, 831, L12

Lyra, W., & Lin, M.-K. 2013, *ApJ*, 775, 17

Marino, S., Perez, S., & Casassus, S. 2015, *ApJL*, 798, L44

Mendigutía, I., Fairlamb, J., Montesinos, B., et al. 2014, *ApJ*, 790, 21

Mittal, T., & Chiang, E. 2015, *ApJL*, 798, L25

Muto, T., Tsukagoshi, T., Momose, M., et al. 2015, *PASJ*, 67, 122

Muzerolle, J., Allen, L. E., Megeath, S. T., Hernández, J., & Gutermuth, R. A. 2010, *ApJ*, 708, 1107

Pérez, L. M., Isella, A., Carpenter, J. M., & Chandler, C. J. 2014, *ApJL*, 783, L13

Rodigas, T. J., Follette, K. B., Weinberger, A., Close, L., & Hines, D. C. 2014, *ApJL*, 791, L37

Rybicki, G. B., & Lightman, A. P. 1979, *New York, Wiley-Interscience*, 1979. 393 p.,

Skrutskie, M. F., Dutkevitch, D., Strom, S. E., et al. 1990, *AJ*, 99, 1187

Strom, K. M., Strom, S. E., Edwards, S., Cabrit, S., & Skrutskie, M. F. 1989, *AJ*, 97, 1451  
Tazaki, R., Tanaka, H., Okuzumi, S., Kataoka, A., & Nomura, H. 2016, *ApJ*, 823, 70  
van den Ancker, M. E., de Winter, D., & Tjin A Djie, H. R. E. 1998, *A&A*, 330, 145  
van der Marel, N., van Dishoeck, E. F., Bruderer, S., et al. 2013, *Science*, 340, 1199  
van der Marel, N., van Dishoeck, E. F., Bruderer, S., et al. 2016, *A&A*, 585, A58  
Verhoeff, A. P., Min, M., Pantin, E., et al. 2011, *A&A*, 528, A91  
Williams, J. P., & Cieza, L. A. 2011, *ARA&A*, 49, 67  
Zhu, Z., & Stone, J. M. 2014, *ApJ*, 795, 53